

Supporting Information

for *Adv. Funct. Mater.*, DOI: 10.1002/adfm.202200660

Field-Free Magnetization Switching Driven by Spin–Orbit
Torque in $L1_0$ -FeCrPt Single Layer

Haochang Lyu, Yunchi Zhao, Jie Qi, He Huang, Jingyan
Zhang, Guang Yang, Yaqin Guo, Shipeng Shen, Weidu
Qin, Young Sun, Jianxin Shen, Pengwei Dou, Bokai
Shao, Yi Zhang, Kui Jin, Youwen Long, Hongxiang Wei,
Baogen Shen, and Shouguo Wang**

Supporting Information

Field-free Magnetization Switching Driven by Spin-Orbit Torque in $L1_0$ -FeCrPt Single Layer

*Haochang Lyu^{1, 2, †}, Yunchi Zhao^{2, †, *}, Jie Qi¹, He Huang¹, Jingyan Zhang¹, Guang Yang³, Yaqin Guo⁴, Shipeng Shen⁴, Weidu Qin⁴, Young Sun⁵, Jianxin Shen¹, Pengwei Dou¹, Bokai Shao¹, Yi Zhang¹, Kui Jin^{2, 6}, Youwen Long^{2, 6}, Hongxiang Wei², Baogen Shen², and Shouguo Wang^{1*}*

¹Beijing Advanced Innovation Center for Materials Genome Engineering, School of Materials Science and Engineering, University of Science and Technology Beijing, Beijing 100083, China

²Beijing National Laboratory for Condensed Matter Physics, Institute of Physics, Chinese Academy of Sciences, Beijing 100190, China

³School of Integrated Circuit Science and Engineering, Beihang University, Beijing, 100191, China

⁴Institute of Advanced Materials, Beijing Normal University, Beijing 100875, China

⁵Center of Quantum Materials and Devices, Chongqing University, Chongqing 401331, China

⁶Songshan Lake Materials Laboratory, Dongguan, Guangdong 523808, China

E-mail: yczhao@iphy.ac.cn; sgwang@ustb.edu.cn

[†]These authors contributed equally to this work

S1. Structural properties and chemical ordering degree of $L1_0$ -Fe_{50-x}Cr_xPt₅₀ films

S2. Magnetic measurements of $L1_0$ -Fe_{50-x}Cr_xPt₅₀ films

S3. Current induced magnetization switching in $L1_0$ -FePt

S4. Cr concentration dependence of transport performance

S5. The effective field correlated to DMI in $L1_0$ -Fe_{50-x}Cr_xPt₅₀ single layer.

S6. Determination of anisotropy field H_k in $L1_0$ -Fe_{50-x}Cr_xPt₅₀ structures

S7. Planar Hall effect measurements for FeCrPt films

- S8. Harmonic measurements for spin-orbit effective field
- S9. Thermal electric effect during measurements
- S10. Small Joule heating in current-induced magnetization switching
- S11. Angular-dependent field-free critical switching current
- S12. First-principles calculations analysis for exchange coupling strength and magnetic anisotropy energy related to Cr doping concentrations

S1. Structural properties and chemical ordering degree of $L1_0$ -FeCrPt.

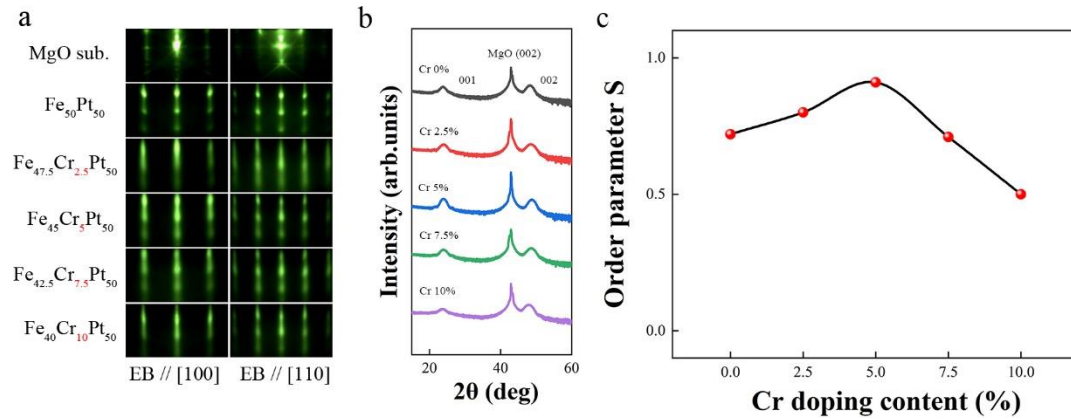


Figure S1 **a** RHEED patterns of MgO substrates and Fe_{50-x}Cr_xPt₅₀ films (x = 0, 2.5, 5, 7.5, 10) with e-beam along with MgO [100] and [110] direction, respectively. **b** XRD spectra of Fe_{50-x}Cr_xPt₅₀ films. **c** Cr content dependence of order parameter S in L₁₀-FeCrPt films.

The reflection high-energy electron diffraction (RHEED) patterns for films with various Cr concentrations are depicted in **Figure S1a**, where the prominent and sharp streaks verify the high quality of the prepared samples. The properties of FeCrPt related to the crystal structure were characterized using X-ray diffraction (XRD). As displayed in **Figure S1b**, the reference FePt sample exhibited pronounced (001) superstructure and (002) reflections, which is a characteristic for the chemically ordered L₁₀-FePt structure. Upon the addition of Cr, no apparent variations of diffractograms were observed and the L₁₀ structure was maintained at all instances. Although the (001) superstructure and (002) reflection position moved leftward with the increasing Cr concentrations, this can be ascribed to the lattice parameter *c* approaching L₁₀-CrPt as the Cr contents continuously increased. Subsequently, the chemical ordering parameter was calculated with the integrated intensity of (001) and (002) diffraction peaks following $S = 0.85 \times \sqrt{I_{001}/I_{002}}$ ^[1]. The calculated chemical ordering parameters obtained from the XRD data for FeCrPt films with varying Cr concentrations are presented in Figure S1c, which suggested a nonmonotonic correlation dependent on the Cr content. Remarkably, the peak chemical ordering parameter emerged for the FeCrPt films with 5% Cr doping.

S2. Magnetic measurements of $L1_0$ -Fe_{50-x}Cr_xPt₅₀ films

The M–H loop of the 5-nm-thick $L1_0$ -Fe₄₅Cr₅Pt₅₀ film measured using vibrating sample magnetometer is portrayed in **Figure S2a**, which indicates a strong perpendicular magnetic anisotropy (PMA). The saturation magnetizations of $L1_0$ -Fe_{50-x}Cr_xPt₅₀ films with varying Cr-doping contents are presented in **Figure S2b**, which exhibits a diminishing trend with the increasing Cr content. Overall, this trend is consistent with the results reported earlier.

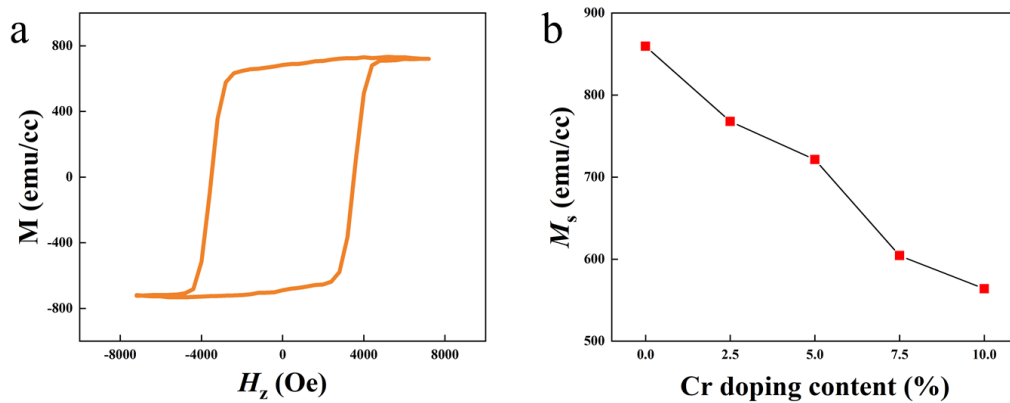


Figure S2 a Magnetization curve of 5-nm-thick $L1_0$ -Fe₄₅Cr₅Pt₅₀ film. **b** Saturation magnetization of $L1_0$ -Fe_{50-x}Cr_xPt₅₀ films with varying Cr doping contents.

S3. Current-induced magnetization switching in $L1_0$ -FePt.

In the presence of required external field in pure $L1_0$ -FePt structure caused by the composition gradient after the application of current, the SOT-induced magnetization switching is presented in **Figure S3a**. The results from the switching experiment are presented in **Figure S3b**. With an in-plane magnetic field ($H_x = -1000$ Oe) applied opposite to the current direction, an anticlockwise loop was observed by sweeping I_p . In particular, the polarity of the switching loop reversed with the reversed magnetic field ($H_x = +1000$ Oe), demonstrating a typical current-induced switching behavior. However, an extremely weak switching was observed at the instant of removing the external magnetic field, and the switching signal completely disappeared upon applying a negative field of only ~100 Oe. Reasonably, this can be attributed to a DMI effective field H_{DMI} related to the composition gradient according

to the recent study of CoTb. However, even in case of a DMI effective field, a desirable SOT switching cannot be achieved owing to the requirement for a larger effective field in the $L1_0$ -FePt structures.

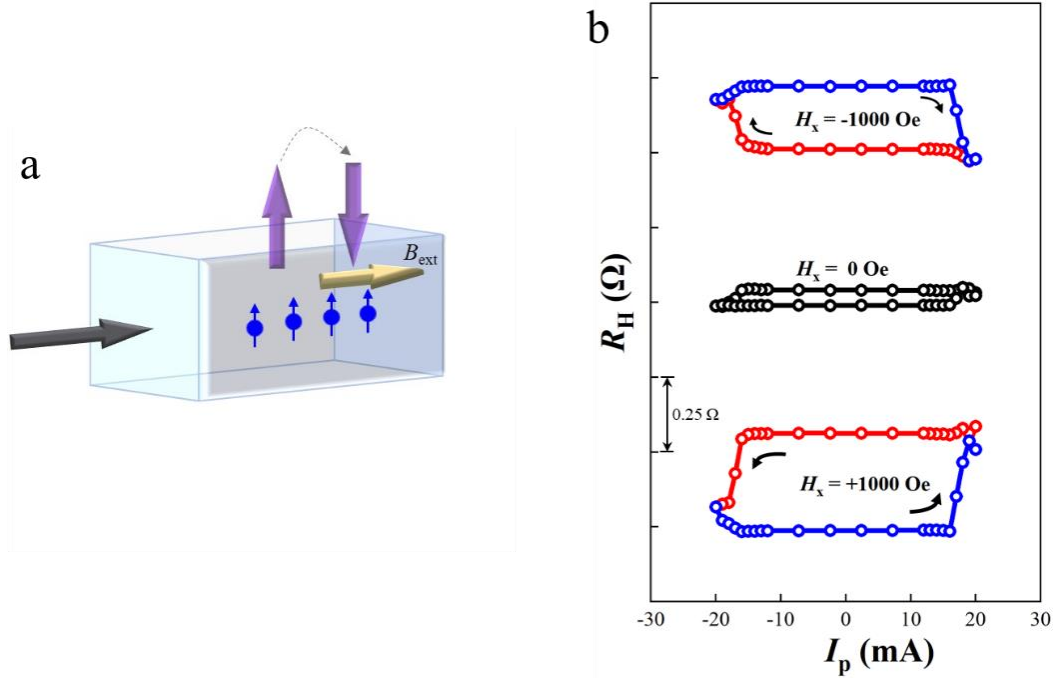


Figure S3 a Schematic of SOT switching in presence of required external field in $L1_0$ -FePt structure owing to the broken structural inversion symmetry induced by composition gradient. **b** SOT switching loops under in-plane magnetic fields of $H_x = -1000$ Oe, 0 Oe, and $+1000$ Oe (from up to down), respectively.

S4. Cr concentration dependence of transport performance

The anomalous Hall effect (AHE) loops were performed by sweeping magnetic field along the normal direction of all films. The AHE loops for $\text{Fe}_{50-x}\text{Cr}_x\text{Pt}_{50}$ samples with varying Cr contents are presented in **Figure S4a**, demonstrating that the PMA is retained until the addition of up to 10% Cr. The excessive Cr concentrations ($> 12.5\%$) results in the magnetic moment of Fe atoms favoring in plane, consistent with the report by Schmidt. As the Cr doping concentration increased, the corresponding coercive fields decreased monotonically and disappeared at Cr contents up to 12.5%, as depicted in **Figure S4b**. On the contrary, increasing Cr concentrations significantly enhances the anomalous Hall resistivity of $\text{Fe}_{50-x}\text{Cr}_x\text{Pt}_{50}$ films, as portrayed in **Figure**

S4c, which is beneficial to the readability in application as sensors and storages.

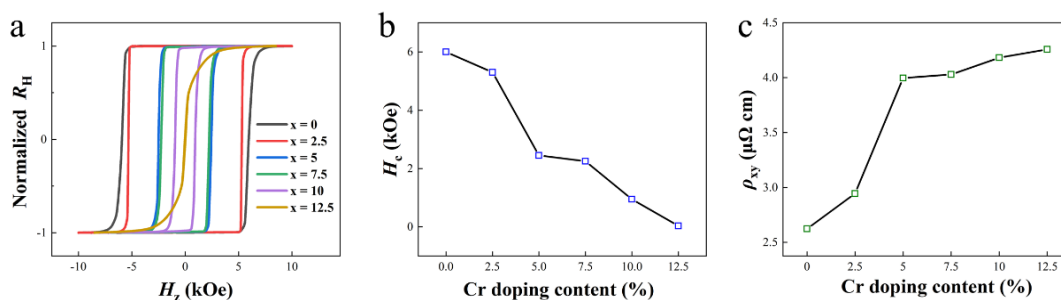


Figure S4 **a** Anomalous Hall loops for FeCrPt films with various Cr concentrations. **b** Coercive field and **c** Anomalous Hall resistivity as a function of Cr doping content.

S5. Effective field correlated to DMI in $L1_0$ -Fe $_{50-x}$ Cr $_x$ Pt $_{50}$ single layer

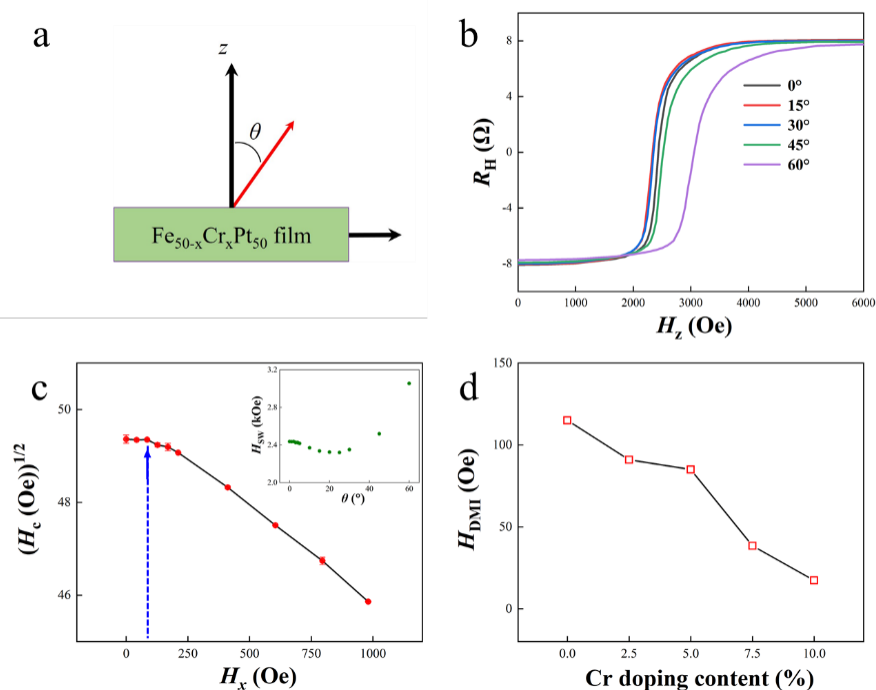


Figure S5 **a** Definition of θ in xz plane during measurements. **b** AHE curves when magnetization switches from up to down under varying magnetic field angles θ with respect to the normal direction of the film. **c** $(H_c)^{1/2}$ as a function of H_x obtained for $Fe_{45}Cr_5Pt_{50}$ films. Above the threshold value of H_x (≈ 87 Oe), H_c starts to decrease. Inset: magnetization switching field H_{sw} with respect to tilted angle θ . **d** H_{DMI} as a function of Cr doping content.

The method based on the magnetic droplet nucleation model was used to quantify the DMI-induced effective field H_{DMI} in all films. As depicted in **Figure S5a**, the hysteresis loops were measured by sweeping the magnetic fields at a tilted angle

with respect to the z -axis. The tilted angle of θ can be defined according to the $+z$ -direction to the $+x$ -direction. The magnetization switching curves in the positive field range with varying θ are illustrated in **Figure S5b**, where the magnetization switching field H_{SW} can be obtained. The measured $(H_c)^{1/2}$ as a function of H_x obtained for $\text{Fe}_{45}\text{Cr}_5\text{Pt}_{50}$ films are presented in **Figure S5c**, where the inset depicts H_{SW} with respect to θ . The coercivity field H_c and the in-plane magnetic field H_x can be expressed as $H_c \equiv H_{\text{SW}}\cos\theta$ and $H_x \equiv H_{\text{SW}}\sin\theta$, respectively. The tendency of $(H_c)^{1/2}$ with respect to H_x was consistent with the results reported in the literature, and it exhibited a threshold point of H_x corresponding to H_{DMI} (indicated by blue arrow). The Cr content dependence of DMI field H_{DMI} is portrayed in **Figure S5d** with this method, thereby following a monotonic reduction in H_{DMI} with Cr content. This result indicated that the bulk DM interaction was suppressed with the introduction of Cr.

S6. Determination of anisotropy field H_k in $L1_0\text{-Fe}_{50-x}\text{Cr}_x\text{Pt}_{50}$ structures

The PMA field was obtained from measuring AHE by sweeping magnetic fields along the hard axis. The illustration of measurements is presented in **Figure S6a**. The AHE loops with $\alpha_H = 2^\circ$ for $\text{Fe}_{45}\text{Cr}_5\text{Pt}_{50}$ sample are depicted in **Figure S6b**. As $V_H \propto V_{\text{AHE}} M_z$, the normalized M_z can be equally acquired by normalizing the AHE signal. Thereafter, the normalized M_x was derived from the relation: $M_x = \sqrt{1 - M_z^2}$. The extracted M_x versus H is illustrated in **Figure S6c**. In addition, the perpendicular anisotropy field H_k was estimated as the field at which the normalized $M_x = 0.98$, as denoted by the blue line. The dependence of the extracted H_k on the Cr content is indicated in **Figure S6d**, which exhibited a diminishing trend with the Cr doping. This indicated that the addition of Cr reduced the barrier from the magnetic anisotropy energy to realize a feasible switching.

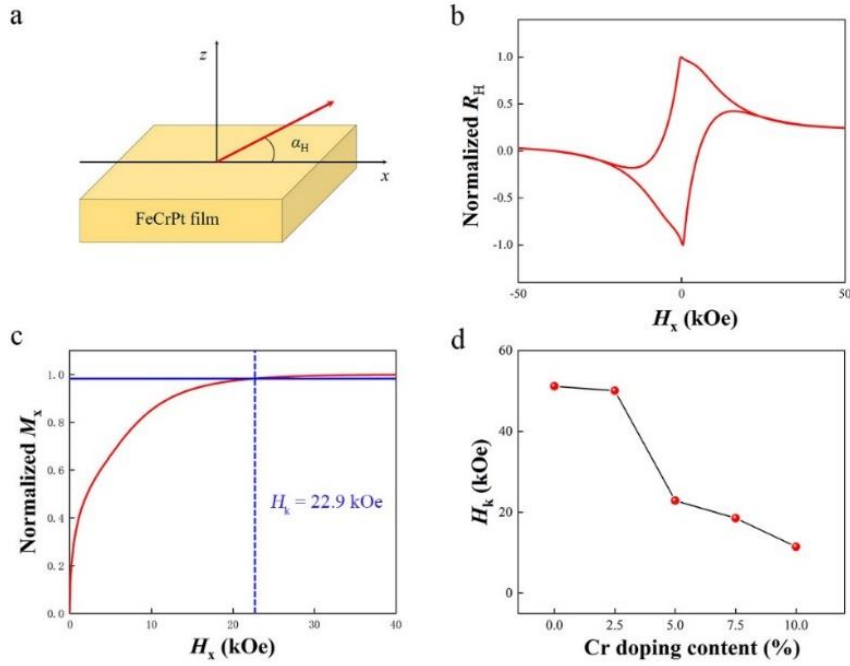
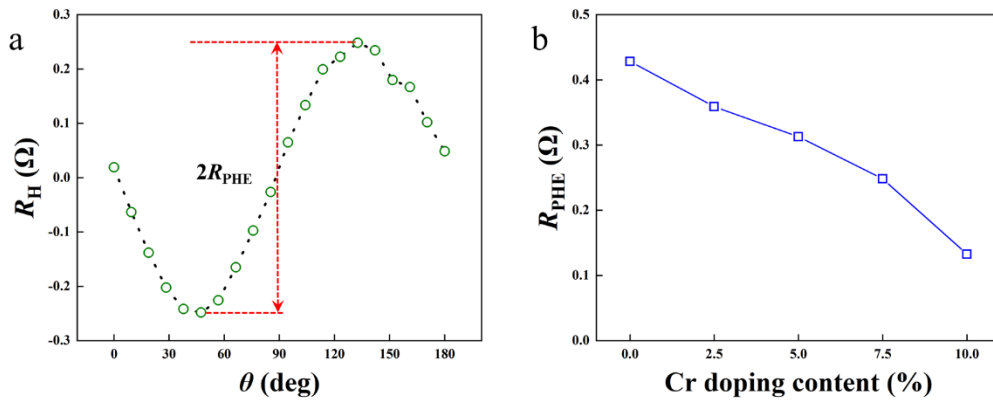


Figure S6 **a** Schematic of measurements. **b** Anomalous Hall loops of a 5-nm-thick $\text{Fe}_{45}\text{Cr}_5\text{Pt}_{50}$ layer by sweeping fields along direction with $\alpha_H = 2^\circ$. AC current of $I = 3$ mA was applied. **c** Normalized M_x versus H (red line) extracted from data of loop with $\alpha_H = 2^\circ$ in **b**. Horizontal blue line indicates normalized $M_x = 0.98$ and vertical blue dash line displays H_k . **d** Dependence of H_k on Cr content.



S7. Planar Hall effect measurements for FeCrPt films

Figure S7 **a** R_H as a function of θ under 9T magnetic field for $\text{Fe}_{45}\text{Cr}_5\text{Pt}_{50}$ films, where θ is defined as the angle between electric current and in-plane magnetic field. **b** R_{PHE} as a function of Cr doping content in FeCrPt films.

The planar Hall effect was reviewed by the in-plane rotation under a large

magnetic field ($H > H_K$), as depicted in **Figure S7a**. The extracted R_{PHE} is presented in **Figure S7b** as a function of Cr doping content, where R_{PHE} decreased with the increasing Cr doping content. In particular, ξ is defined as the ratio of planar Hall voltage to the anomalous Hall voltage, the value of ξ for Cr doping content of 0, 2.5%, 5%, 7.5%, 10% was 0.082, 0.061, 0.039, 0.031, and 0.016, respectively. These results further confirm the negligibility of R_{PHE} for FeCrPt films.

S8. Harmonic measurement for spin orbit effective field with varying Cr contents

To quantitatively investigate the spin orbit efficiency in $L1_0$ -ordered FeCrPt films, the harmonic measurements were conducted by sweeping in-plane magnetic fields H_x (parallel to the current direction) at room temperature. The first V_ω and second $V_{2\omega}$ harmonic Hall voltages of $L1_0$ -FeCrPt film were detected using two lock-in amplifiers simultaneously. Prior to the harmonic measurements, a large extent of the out-of-plane external field was applied to saturate the sample, which was maintained till the field was removed. As indicated in Figure S8a, the first (V_ω) and second ($V_{2\omega}$) harmonic Hall signals for the sample with 5% Cr doping under in-plane magnetic fields ranged from -3000 Oe to $+3000$ Oe. As observed in Figure S8b, H_L can be derived as a linear function of alternating current with varying Cr contents, and Equation (1) from the main text exhibits a good fitting with the curve of this function; the corresponding slope reflects the magnitude of the spin orbit efficiency.

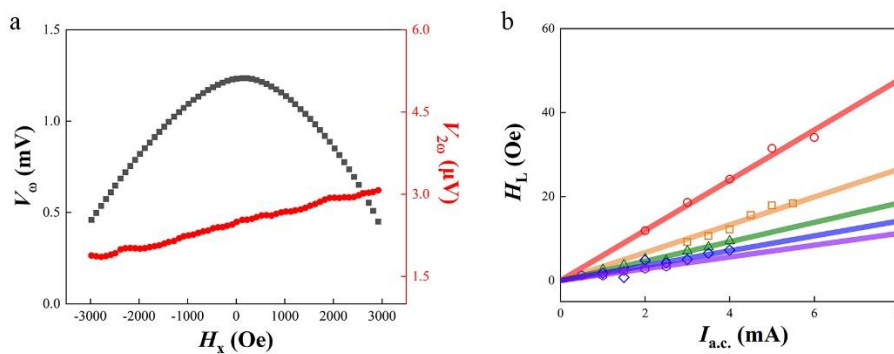


Figure S8 a First V_ω (black) and second $V_{2\omega}$ (red) harmonic Hall voltages signals of 5-nm-thick $L1_0$ -FeCrPt film. **b** H_L as a linear function of alternating current with varying Cr contents.

S9. Thermoelectric effect during measurements

The second harmonic Hall signals can be influenced by thermoelectric effects.

As illustrated in Figure S9a, a temperature gradient is generated from various directions (T_x , T_y , and T_z) when the current flows through Hall bar. Longitudinal gradient T_x and transverse T_y in the film plane fundamentally evolves from the inhomogeneous heating caused by the fabrication defects on the corner of the devices, whereas T_z arises from the asymmetric heat dissipation toward the air and MgO substrate. Consequently, a charge imbalance will be generated by the temperature gradient because of the anomalous Nernst effect (ANE) and spin Seebeck effect (SSE).

For the temperature gradients generated in the film plane (T_x and T_y), their contributions toward the second harmonic signals can be measured from the sweeping magnetic fields along the z -axis (normal to the film plane). As portrayed in **Figure S9b**, $V_{2\omega}$ signals of the FeCrPt film with Cr concentrations of 5% was measured by sweeping magnetic fields along the z -axis. The estimated R_{ANE} from in-plane ANE contribution was $0.36 \text{ m}\Omega$ ($V_{ANE} = 0.54 \text{ }\mu\text{V}$). The central value of the loop primarily arises from the misalignment of the Hall voltage leads and the SSE, which is the offset signal $V_{2\omega, \text{Offset}}$ ($-2.75 \text{ }\mu\text{V}$). Both V_{ANE-IP} and $V_{2\omega, \text{Offset}}$ contribute to the second harmonic signals for the sweeping in-plane fields. On the contrary, V_{ANE-IP} and $V_{2\omega, \text{Offset}}$ only provide an overall constant offset to the second harmonic signals, which does not govern the slope of $V_{2\omega}$, as consistent with other studies^[2,3]. Thus, the in-plane temperature gradients have no dramatic influence on the result of effective spin-torque fields.

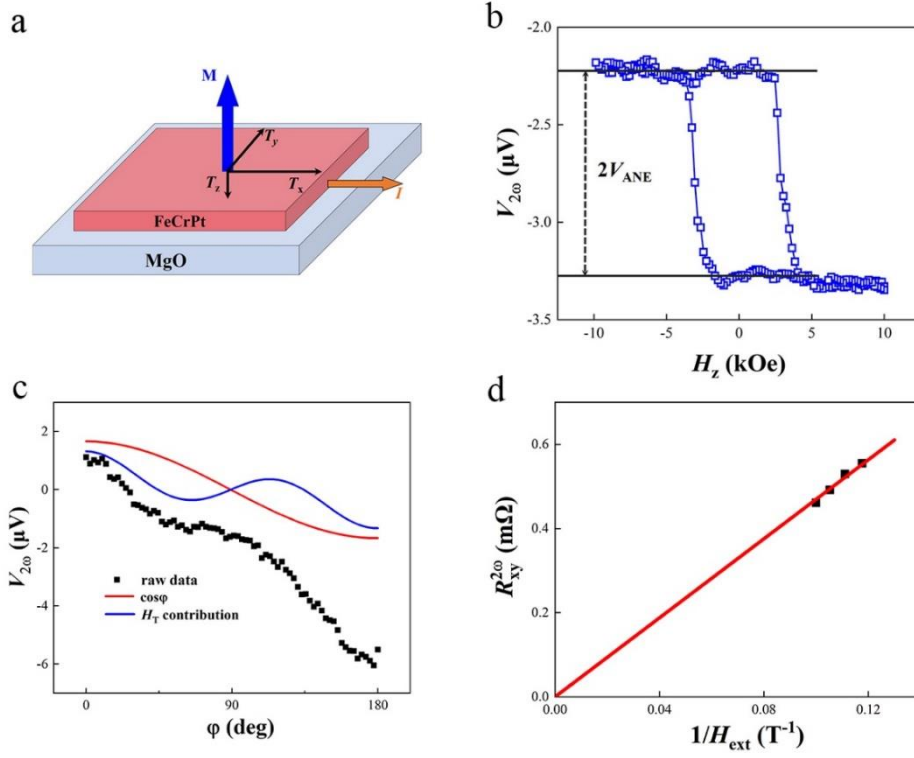


Figure S9 **a** Schematic of temperature gradient generated in film plane by in-plane current. **b** $V_{2\omega}$ plotted against large external fields H_z in $\text{Fe}_{45}\text{Cr}_5\text{Pt}_{50}$ film. **c** In-plane angle (from x - to y -axes) dependence of second-harmonic transverse voltage in $\text{Fe}_{45}\text{Cr}_5\text{Pt}_{50}$ with external field of 9 T. **d** $R_L^{2\omega} + R_{VT}^{2\omega}$ as a function of inverse of external fields against current-induced field.

More importantly, the temperature gradient generated perpendicular to the film (T_z) produces ANE and SSE in case of an in-plane magnetization. Thus, to estimate the thermal contribution (ANE and SSE) from T_z , the harmonic Hall voltages of $\text{Fe}_{45}\text{Cr}_5\text{Pt}_{50}$ sample with varying magnetic fields rotating in the xy -plane according to the following equation^[4]:

$$V_{xy}^{2\omega} = \left[\left(V_{AHE} \frac{H_L}{H_{ext}} + I_0 \alpha \nabla T \right) \cos \phi + 2V_{PHE} (2\cos^3 \phi - \cos \phi) \frac{H_T + H_{Oe}}{H_{ext}} \right], \quad (1)$$

where both $V_L^{2\omega}$ and $V_{VT}^{2\omega}$ are proportional to $\cos \phi$, whereas $V_T^{2\omega}$ is proportional to $(2\cos^3 \phi - \cos \phi)$. Therefore, the contribution of longitudinal torque, transverse torque, and thermoelectric effect can be separated by measuring the in-plane angle ϕ (from x - to y -axes) dependence of $V_{xy}^{2\omega}$ on vast external fields. The angle dependence of the second-harmonic transverse voltages with an external field of 9 T is portrayed in **Figure S9c**. As observed, the longitudinal torque and thermoelectric terms are

included within the $\cos\varphi$ -like term, which is reflected in the plot of a linear function of $R_L^{2\omega} + R_{\nabla T}^{2\omega}$ with respect to $1/H_{ext}$, as expressed in Figure S9d. The longitudinal torque term can be approximately represented by the slope of the fitted line, and the intercept corresponds to the thermoelectric term approaching zero. Therefore, the contribution involving the thermoelectric effect from T_z can be neglected as well.

S10. Small Joule heating in current-induced magnetization switching

The “pulse + equilibrium” mode^[5] was recording using a small DC current of 500 μA , and a long pulse delay of 10 s was used to minimize the thermal effects. The variations in the longitudinal resistance R_{xx} during SOT switching are depicted in **Figure S10**, where a minor response yields a small variation in temperature of SOT switching in $L1_0$ -FeCrPt. This demonstrates a negligible effect of thermal effect on the SOT-switching measurements. In addition, the SOT effective field was measured by the harmonic Hall voltage analysis under low ac currents to minimize the thermal effects. Therefore, the thermal effect in $L1_0$ -FeCrPt was negligibly small, and its effect on the estimation of effective field can be neglected.

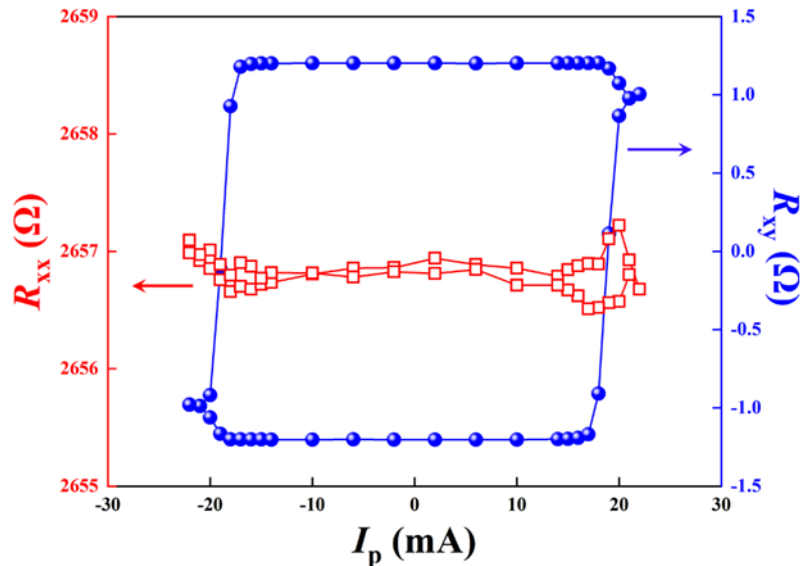


Figure S10 Variations in R_{xx} corresponding to SOT switching.

S11. Angular-dependent field-free critical switching current.

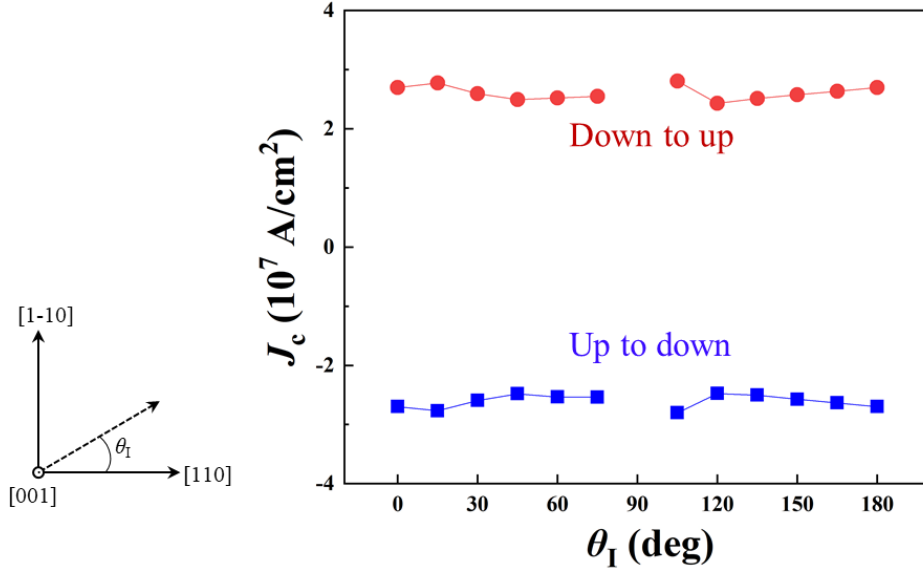


Figure S11 Angular-dependent field-free critical switching current.

Zhao et al.^[6] detected an asymmetric SOT-induced switching between up-to-down and down-to-up magnetized states in Ta/CoFeB/MgO multilayers in case the assisting field direction was noncollinear with the electric current, and attributed it to the large transverse SOT effective field, thereby revealing the vitality of the transverse SOT effective field on the magnetization switching. For SOT switching in FeCrPt, the assisting field can be replaced with the in-plane effective field. Therefore, the field-free angular dependence of SOT switching current density J_c can be investigated, as presented in **Figure S11**, where θ_I is defined as the angle between the electric current direction and the FeCrPt [110] crystal axis. J_c denotes a symmetric SOT switching feature instead of the asymmetric switching behavior in Ta/CoFeB/MgO films. Compared to those conventional angular-dependent switching with an applied external field, it is independent of angular orientation, suggesting that the intrinsic in-plane effective field is less influential on the magnitude of J_c .

S12. First-principles calculation for exchange coupling strength and magnetic anisotropy energy related to Cr doping concentrations.

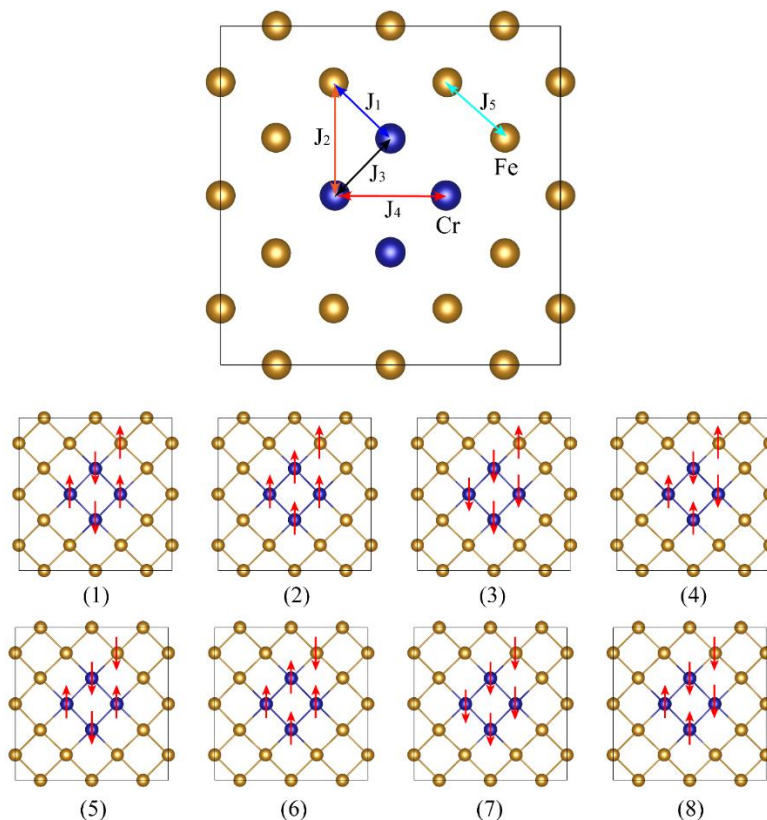


Figure S12 Clustered Cr (paired Cr). Exchange paths for nearest and next-nearest neighbor Cr-Cr and Cr-Fe, and only nearest neighbor Fe-Fe pairs. (1)-(8) exhibits magnetic configuration utilized here. All Fe atoms are assumed at pristine spin-up polarization. Yellow and blue balls represent Fe and Cr atoms, respectively.

Two models including paired and isolated Cr atoms were considered based on first-principles calculation. All calculations in this study were adopted by the density functional theory (DFT) implemented in the Vienna *Ab-initio* simulation package (VASP)^[7] by utilizing the generalized gradient approximation (GGA) with the Perdew-Burke-Ernzerhof (PBE) functional^[8,9]. Specifically, we constructed a $3 \times 3 \times 1$ $L1_0$ -FePt supercell with four centrosymmetric Cr substitution of Fe atoms introduced to simulate the exchange coupling between the Cr-Cr and Cr-Fe couples, as illustrated in **Figure S12**.

The threshold energy was set to 520 eV and a $3 \times 3 \times 13$ Γ -center k-point grid was sampled. The pristine structure was completely relaxed until the electronic

iteration energy and Hellmann–Feynman force on each atom reached 10^{-6} eV and $0.01 \text{ eV}\cdot\text{\AA}^{-1}$, respectively. All calculations were spin-polarized with the consideration of the magnetic configurations enumerated in Figure S12.

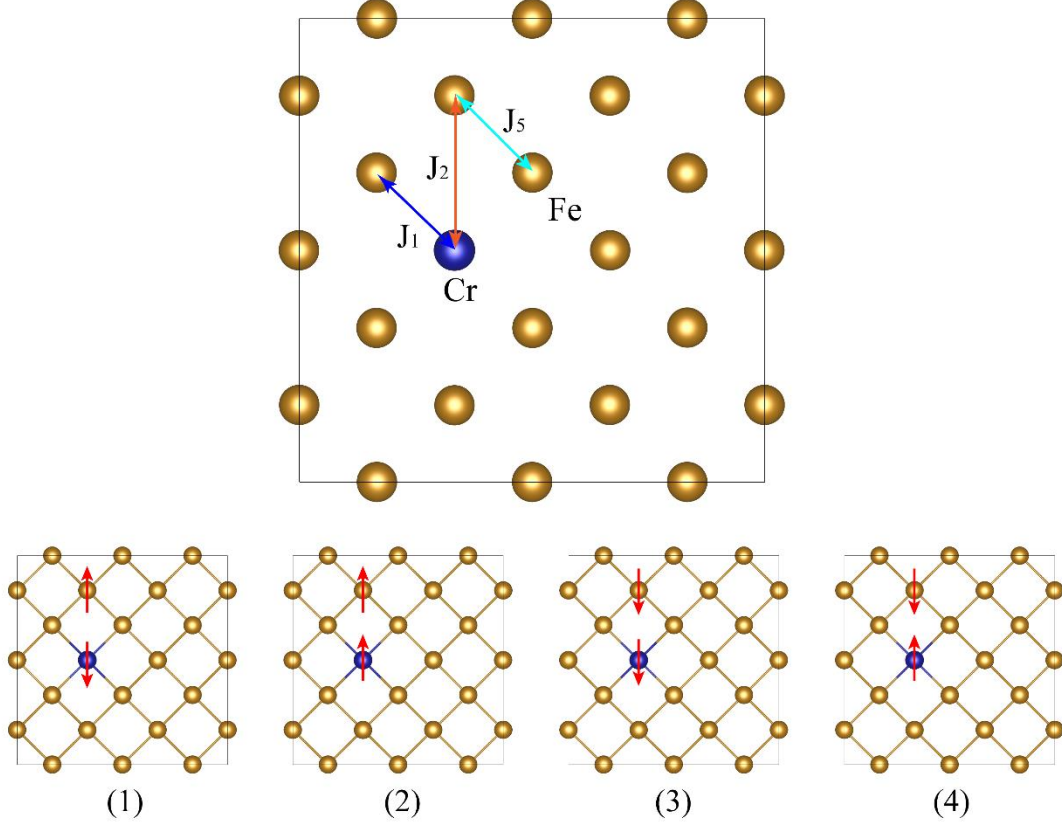


Figure S13 Isolated Cr. Exchange paths for nearest and next-nearest neighbor Cr-Cr and Cr-Fe, and only nearest neighbor Fe-Fe pairs. (1)-(4) exhibit the magnetic configurations utilized here. All Fe atoms are assumed at pristine spin-up polarization. Yellow and blue balls represent Fe and Cr atoms, respectively.

The classical Heisenberg spin Hamiltonian can be expressed as

$$H = E_0 + J_k \sum_{\langle i,j \rangle} S_i S_j, \quad (2)$$

where E_0 represents the energy without magnetic coupling deviation in the calculations, J_k denotes the exchange coupling of the nearest- and next-nearest neighbor Cr–Cr and Cr–Fe, and only nearest neighbor considered Fe–Fe pairs displayed in **Figure S13**, wherein the positive and negative J values indicate FM and AFM coupling, respectively. All exchange parameters were approximatively derived from the energy mapping of the listed magnetic configurations:

$$H(1) = E_0 + 4J_3 - 2J_4 - 3J_5$$

$$H(2) = E_0 - 4J_3 - 2J_4 - 8J_1 - 12J_2 - 3J_5$$

$$H(3) = E_0 - 4J_3 - 2J_4 + 8J_1 + 12J_2 - 3J_5$$

$$H(4) = E_0 + 2J_4 - 3J_5$$

$$H(5) = E_0 + 4J_3 - 2J_4 - 2J_1 + 2J_2 + 3J_5$$

$$H(6) = E_0 - 4J_3 - 2J_4 - 6J_1 - 10J_2 + 3J_5$$

$$H(7) = E_0 - 4J_3 - 2J_4 + 6J_1 + 10J_2 + 3J_5$$

$$H(8) = E_0 + 2J_4 - 2J_1 - 2J_2 + 3J_5$$

After calculations, J_1 , J_2 , J_3 and J_4 were determined as -83.5 , 4.8 , -115.2 , and 33.7 meV, respectively.

In Figure S13,

$$H(1) = E_0 + 4J_1 + 4J_2 - 4J_5$$

$$H(2) = E_0 - 4J_1 - 4J_2 - 4J_5$$

$$H(3) = E_0 + 4J_1 + 2J_2 + 4J_5$$

$$H(4) = E_0 - 4J_1 - 2J_2 + 4J_5$$

As computed, J_1 and J_2 equal to -98.6 meV and 13.2 meV, respectively.

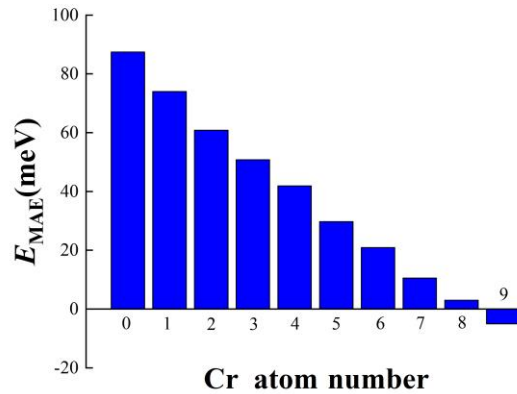


Figure S14. MAE of $Fe_{50-x}Cr_xPt_{50}$ films as a function of doped Cr atoms.

Furthermore, Cr-doped $Fe_{50-x}Cr_xPt_{50}$ films were modeled in the bulk $4 \times 4 \times 1$ geometry. Based on a second-order perturbation theory^[10], the MAE can be obtained by calculating the total energy difference between out-of-plane and in-plane magnetization orientation, where the positive and negative values represent the perpendicular magnetic anisotropy (PMA) and in-plane magnetic anisotropy (IMA),

respectively. As observed from Figure S14. the amplitude of magnetic anisotropy energy (MAE) decreased from 87.4 to -5 meV with the increasing Cr content.

References

- [1] C. B. Rong, D. Li, V. Nandwana, N. Poudyal, Y. Ding, Z. L. Wang, H. Zeng, J. P. Liu. *Adv. Mater.* **2006**, 18, 2984.
- [2] L. Liu, J. H. Yu, R. González-Hernández, C. J. Li, J. Y. Deng, W. N. Lin, C. H. Zhou, T. J. Zhou, J. Zhou, H. Wang, R. Guo, H. Y. Yoong, G. M. Chow, X. F. Han, B. Dupé, J. Železný, J. Sinova, J. S. Chen. *Phys. Rev. B* **2020**, 101, 220402.
- [3] S. Q. Zheng, K. K. Meng, Q. B. Liu, J. K. Chen, J. Miao, X. G. Xu, Y. Jiang. *Appl. Phys. Lett.* **2020**, 117, 242403.
- [4] C. O. Avci, K. Garelo, M. Gabureac, A. Ghosh, A. Fuhrer, S. F. Alvarado, P. Gambardella. *Phys. Rev. B* **2014**, 90, 224427.
- [5] L. Liu, T. Zhao, L. Ren, C. Zhou, W. Lin, X. Shu, J. Zhou, Q. Xie, J. Chen. *ACS Appl. Electron. Mater.* **2021**, 3, 2483.
- [6] W. Fan, J. Zhao, M. Tang, H. Chen, H. Yang, W. Lü, Z. Shi, X. Qiu. *Phys. Rev. Appl.* **2019**, 11, 034018.
- [7] G. Kresse, J. Furthmuller. *Phys. Rev. B Condens. Matter.* **1996**, 54, 11169.
- [8] M. Ernzerhof, G. E. Scuseria. *J. Chem. Phys.* **1999**, 110, 5029.
- [9] B. Hammer, L. B. Hansen, J. K. Nørskov. *Phys Rev B* **1999**, 59, 7413.
- [10] D. Wang, R. Wu, A. J. Freeman. *Phys. Rev. B Condens. Matter.* **1993**, 47, 14932.